Numerical Heat Transfer, Part A, 39:35–59, 2001
Copyright © 2001 Taylor & Francis
1040-7782/01 $12.00 + .00

SIMULATION OF TURBULENT FLOW IN POROUS MEDIA USING A SPATIALLY PERIODIC ARRAY AND A LOW RE TWO-EQUATION CLOSURE

Marcos H. J. Pedras
Instituto de Pesquisa e Desenvolvimento IP&D, UNIVAP, São José dos Campos-SP, Brazil

Marcelo J. S. de Lemos
Departamento de Energia—IEME, Instituto Tecnológico de Aerânautica—ITA, 12228-900—São José dos Campos—SP, Brazil

A spatially periodic array is used to simulate the turbulent flow field inside an elementary control volume representing a porous medium. The low Reynolds (Re) version of the $k-\varepsilon$ model is employed. Mean flow and turbulence equations are discretized by means of the control-volume approach. Boundary treatment includes symmetry lines and spatially periodic conditions. A generalized coordinate system is used to generate the computational grid. Solution of the flow equations is accomplished through the SIMPLE method. Detailed computations are used to close the proposed macroscopic turbulence model. Overall pressure drop and volume-averaged turbulence kinetic energy (TKE) are presented. For the condition analyzed here the integral turbulence energy increases with reduction of the medium porosity.

INTRODUCTION

There has been great interest lately regarding turbulent flow in porous media. This is certainly related to the number of engineering systems having some sort of porous structure through which a working fluid permeates. Transition to a turbulent regime in the vicinity of oil wells, within large voids caused by the continuous erosion because of oil flow, may affect the overall head loss. Fluidized bed combustors when subjected to a large incoming air flow required to attain to momentary power production increase also can be subjected to variations of pressure loss because of changes in the flow regime.

When the pore Reynolds number Re_p is less than about 150, classical mathematical models for flow in porous media [1–7] are based on a representative elemen-

Received 16 February 2000; accepted 24 August 2000.
M. J. S. de Lemos is thankful to CNPq, Brazil, for its financial support during the course of this research.
Address correspondence to Dr. Marcelo J. S. de Lemos, Depatamento de Energia—IEME, Instituto Tecnológico de Aeronautica—ITA, 12228-900—São José dos Campos—SP, Brazil. E-mail: mdelemos@tecsat.com.br

NOMENCLATURE

c_k	constant in the extra production term for k-equation	$\bar{\mathbf{u}}_D$	Darcy velocity vector
c_μ	constant in the Kolmogorov–Pradtl expression	$\langle\bar{\mathbf{u}}\rangle^i$	intrinsic velocity vector
D	rod diameter	x, y	Cartesian coordinates
H	height of periodic cell	ε	dissipation rate of k, $\varepsilon = \mu\overline{\nabla\mathbf{u}' : (\nabla\mathbf{u}')^T}/\rho$
f_μ	damping function for μ_t	$\langle\varepsilon\rangle^i$	intrinsic (fluid) average for ε
f_ε	damping function for ε-equation	ε_ϕ	fully developed value of $\langle\varepsilon\rangle^i$
k	turbulence kinetic energy (TKE), $k = \overline{\mathbf{u}'\cdot\mathbf{u}'}/2$	ΔV	representative elementary volume
$\langle k\rangle^i$	intrinsic (fluid) aveage for k, $\langle k\rangle^i = \langle\overline{\mathbf{u}'\cdot\mathbf{u}'}\rangle^i/2$	ΔV_f	volume of fluid inside ΔV
k_m	TKE based on the fluctuation of $\langle\bar{\mathbf{u}}\rangle^i$, $k_m = \overline{\langle\mathbf{u}'\rangle^i\cdot\langle\mathbf{u}'\rangle^i}/2$	φ	general variable
k_ϕ	fuly developed value of $\langle k\rangle^i$	ϕ	porosity
K	medium permeability	$\langle\varphi\rangle^i$	intrinsic (fluid) average of φ
n	distance normal to the wall	$^i\varphi$	spatial deviation from intrinsic average of φ
p	pressure	$\mu_{m\phi}$	macroscopic coefficient of exchange for porous media
P	overall pressure, $P = p + 2/3\rho k$	μ_t	turbulent coefficient of exchange
P_k	production term of k	μ	fluid dynamic viscosity
Re_p	pore Reynolds number	ν	fluid kinematic viscosity, $\nu = \mu/\rho$
Re_H	Reynolds number based on H	σ_k	turbulent Prandtl number for $\langle k\rangle^i$
S	length of periodic cell, $S = 2H$	σ_ε	turbulent Prandtl number for $\langle\varepsilon\rangle^i$
S_φ	general source term for $\varphi = U, V, k, \varepsilon$	ρ	fluid density
$\bar{\mathbf{u}}$	microscopic velocity vector		
U, V	Cartesian components of vector $\bar{\mathbf{u}}$		

tary volume (REV; Figure 1*a*) for which balance equations governing momentum, energy, and mass transfer are written. For high Re ($\mathrm{Re}_p > 300$), however, turbulence models presented in the literature follow two basic approaches. In the first method [8–10], governing equations for the mean and turbulent field are obtained by time averaging the volume-averaged equations. In the second approach [11–16], a volume-averaged operator is applied to the local time-averaged equation. The turbulence kinetic energy associated with the flow in the two cases is different [17], and a connection between these two quantities recently has been established [18].

Driven by the need for a better characterization of turbulent flow within such media, we detail a methodology for closing a macroscopic turbulence model for flow through a rigid saturated permeable medium [19]. Adjustment of the proposed model includes solution of the flow governing equation within the periodic computational cell represented in Figure 1*b*. That periodic cell is a representation of the REV as consisting of an infinite array of cylinders. The governing equations are discretized using nonorthogonal coordinates conforming to the void volume occupied by the fluid phase. Integrated parameters then are used in the macroscopic model to close the mathematical problem.

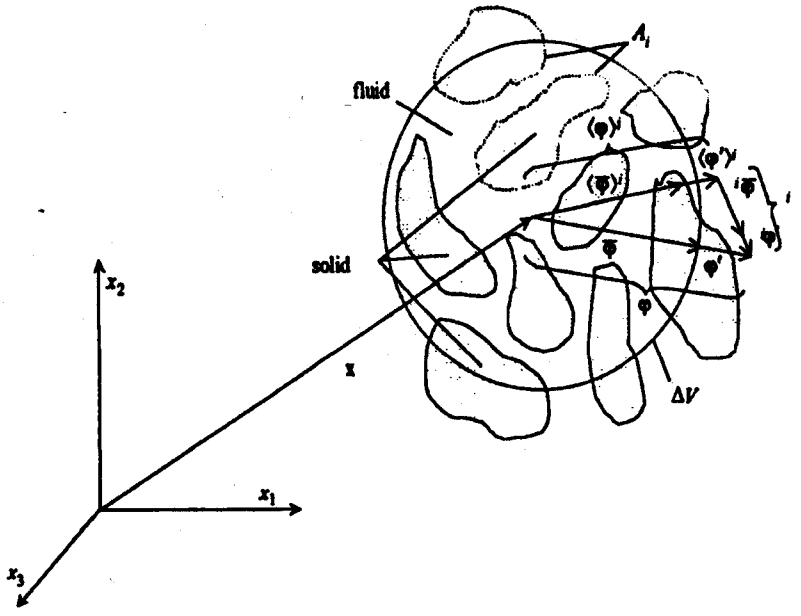

a)

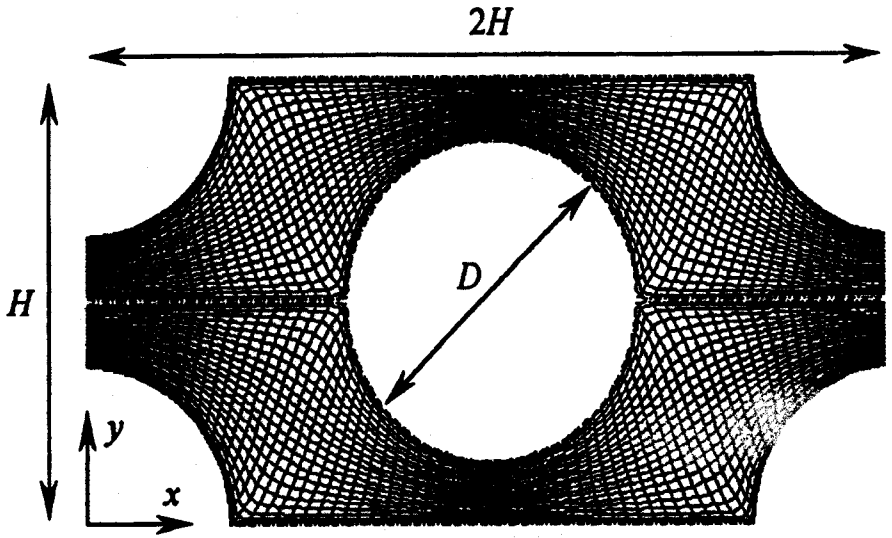

b)

Figure 1. (*a*) Representative elementary volume (REV); (*b*) model of REV, periodic cell, and nonorthogonal grid.

MICROSCOPIC REYNOLDS-AVERAGED NAVIER–STOKES (RANS) EQUATIONS

The RANS equations describe fluid flow in continuum medium. They will be solved in the domain of Figure 1*b*. For the steady state condition they are promptly written as

Continuity

$$\nabla \cdot \bar{\mathbf{u}} = 0 \tag{1}$$

Momentum

$$\nabla \cdot (\rho \bar{\mathbf{u}}\bar{\mathbf{u}}) = -\nabla \bar{p} + \mu \nabla^2 \bar{\mathbf{u}} + \nabla \cdot (-\rho \overline{\mathbf{u}'\mathbf{u}'}) \tag{2}$$

where the stresses, $-\rho \overline{\mathbf{u}'\mathbf{u}'}$, are the well-known Re stresses. The use of the eddy-diffusivity concept for expressing the *stress-rate-of-strain* relationship for the Re stress appearing in (2) gives

$$-\rho \overline{\mathbf{u}'\mathbf{u}'} = \mu_t 2\bar{\mathbf{D}} - \frac{2}{3}\rho k \mathbf{I} \tag{3}$$

where $\bar{\mathbf{D}} = [\nabla \bar{\mathbf{u}} + (\nabla \bar{\mathbf{u}})^T]/2$ is the mean deformation tensor, $k = \overline{\mathbf{u}' \cdot \mathbf{u}'}/2$ is the turbulent kinetic energy per unit mass, and $\mathbf{I}$ is the unity tensor. Applying (3) to (2) gives further

$$\nabla \cdot (\rho \bar{\mathbf{u}}\bar{\mathbf{u}}) = -\nabla\left(\bar{p} + \frac{2}{3}\rho k\right) + \mu \nabla^2 \bar{\mathbf{u}} + \nabla \cdot (\mu_t 2\bar{\mathbf{D}}) \tag{4}$$

The term $(p + 2/3\ \rho k)$ in (4) can be substituted by the total pressure P. To obtain an equivalent expression for the macroscopic Re stress tensor, the volume-averaging operator with respect to ΔV will be carried out in both Eqs. (2) and (4).

The low Re k–ε model. The coefficient μ_t appearing in Eq. (3) is calculated here using the standard low-Re k-ε model and reads:

$$\mu_t = c_\mu \rho f_\mu \frac{k^2}{\varepsilon} \tag{5}$$

where c_μ is a constant. Transport equations for k and ε are given by

$$\nabla \cdot (\rho \bar{\mathbf{u}} k) = \nabla \cdot \left[\left(\frac{\mu_t}{\sigma_k} + \mu\right)\nabla k\right] + S_k; \quad S_k = P_k - \rho\varepsilon \quad P_k = -\rho \overline{\mathbf{u}'\mathbf{u}'} : \nabla \bar{\mathbf{u}} \tag{6}$$

$$\nabla \cdot (\rho \bar{\mathbf{u}} \varepsilon) = \nabla \cdot \left[\left(\frac{\mu_t}{\sigma_\varepsilon} + \mu\right)\nabla \varepsilon\right] + S_\varepsilon; \qquad S_\varepsilon = c_1 P_k \frac{\varepsilon}{k} - c_2 f_\varepsilon \rho \frac{\varepsilon^2}{k} \tag{7}$$

The term P_k is the production rate of k and the damping functions f_μ and f_ε are taken

from Abe et al. [20] as

$$f_\mu = \left\{1 - \exp\left[-\frac{(v\varepsilon)^{0.25} n}{14v}\right]\right\}^2 \left\{1 + \frac{5}{(k^2/v\varepsilon)^{0.75}} \exp\left[-\left(\frac{(k^2/v\varepsilon)}{200}\right)^2\right]\right\} \tag{8}$$

$$f_2 = \left\{1 - \exp\left[1\frac{(v\varepsilon)^{0.25} n}{3.1v}\right]\right\}^2 \left\{1 - 0.3\exp\left[-\left(\frac{(k^2/v\varepsilon)}{6.5}\right)^2\right]\right\} \tag{9}$$

where n is the distance from the nearest wall and v is the kinematic viscosity. The constants used read:

$$c_\mu = 0.09 \quad c_1 = 1.5 \quad c_2 = 1.9 \quad \sigma_k = 1.4 \quad \sigma_\varepsilon = 1.3 \tag{10}$$

To keep a unidirectional value for the volumetric velocity average $\bar{\mathbf{u}}_D$ (Darcy velocity), we imposed the following conditions at the boundaries of the periodic cell of Figure 1:

$$\text{At walls, } \bar{\mathbf{u}} = 0, k = 0, \text{ and } \varepsilon = v\frac{\partial^2 k}{\partial n^2} \tag{11}$$

$$\text{At } y = 0 \text{ and } y = \frac{H}{2} \text{ symmetry line, } \frac{\partial \varphi}{\partial y} = 0, \varphi = \bar{u}, k, \varepsilon$$

At the inlet and outlet periodic boundaries ($x = 0$ and $x = 2H$)

$$U|_{x=0} = U|_{x=2H} \qquad V|_{x=0} = V|_{x=2H} \tag{13}$$

$$k|_{x=0} = k|_{x=2H} \qquad \varepsilon|_{x=0} = \varepsilon|_{x=2H} \tag{14}$$

where U and V are the components of $\bar{\mathbf{u}}$.

Equation (13) entails the periodic boundary condition methodology applied here. In the beginning of the calculations, the flow at the inlet (left side of Figure 1*b*) was set as having a constant U-component along y. Only at the start of calculations the V-component at the inlet position ($x = 0$) was set to zero. After convergence, the outlet profiles for both U and V, on the right side of Figure 1*b*, were fed at the inlet and a new run was started. Computations were once more carried out until convergence was established. Subsequently, the profiles at exit ($x = 2H$) were plugged in again at the inlet and a new run was conducted. The entire process was repeated until no difference between inlet and outlet profiles was detected. Later in this work results for the intermediate nonzero profiles for V at the outlet will be shown.

The set of Eqs. (1)–(4)–(6)–(7) comprises the transport equations necessary for describing the flow in a clear fluid. Additional equations for completing the set are (5)–(8)–(9) and boundary condition imposed on the equations are (11)–(14). All of these equations are discretized in the grid shown in Figure 1*b*.

VOLUME AND TIME-AVERAGED k–ε EQUATIONS

Volume and Time Average

The use of volume and time-averaging procedures for obtaining transport equations for k and ε in porous media is discussed in detail in Refs. [17, 18]. For clarity, the major ideas therein are included here.

The macroscopic governing equation for flow through a porous substratum can be obtained by volume averaging the corresponding microscopic equations over an REV, ΔV [6]. For a general fluid property, φ, the intrinsic and volumetric averages are related through the porosity ϕ as [19, 21]

$$\langle\varphi\rangle^i = \frac{1}{\Delta V_f}\int_{\Delta V_f} \varphi \, dV \quad \langle\varphi\rangle^v = \phi\langle\varphi\rangle^i \quad \phi = \frac{\Delta V_f}{\Delta V} \tag{15}$$

where ΔV_f is the volume of the fluid contained in ΔV. The property φ then can be defined as the sum of $\langle\varphi\rangle^i$ and a term related to its spatial variation within the REV, ${}^i\varphi$, as [5]

$$\varphi = \langle\varphi\rangle^i + {}^i\varphi \tag{16}$$

The spatial deviation is the difference between the real value (microscopic) and its intrinsic (fluid-based average) value.

The need for considering time fluctuations occurs when turbulence effects are of concern. The microscopic time-averaged equations are obtained from the instantaneous microscopic equations. For that, the time-averaged value of property, φ, associated with the fluid is given as

$$\bar{\varphi} = \frac{1}{\Delta t}\int_t^{t+\Delta t} \varphi \, dt \tag{17}$$

where Δt is the integration time interval. The instantaneous property φ can be defined as the sum of the time average, $\bar{\varphi}$, plus the fluctuating component, φ':

$$\varphi = \bar{\varphi} + \varphi' \tag{18}$$

From the definition of volume average (15) and time average (17) and assuming a rigid medium, one can conclude the following properties:

$$\overline{\langle\varphi\rangle^i} = \langle\bar{\varphi}\rangle^i \quad \langle\varphi'\rangle^i = \langle\varphi\rangle^{i\prime} \quad {}^i\bar{\varphi} = \overline{{}^i\varphi} \tag{19}$$

The proofs of identities (19) are found in detail in Pedras and de Lemos [17]. In developing Eqs. (19) the only restriction applied was the independence of ΔV in relation to time and space. If the medium is further assumed to be rigid, then ΔV_f is dependent on space but is not time dependent [17].

With these ideas in mind, a proposition for volume- and time-averaged transport equations for k and ϵ equations can be made.

Model Equation for $\langle k\rangle^i$

An equation for the intrinsic average for the turbulence kinetic energy, $\langle k\rangle^i$, is obtained by applying the volume average operator (15) to the transport equation for k (Eq. (6)). Making use of the Dupuit–Forchheimer relationship, $\bar{\mathbf{u}}_D = \phi\langle\bar{\mathbf{u}}\rangle^i$,

we propose a model [22, 23]

$$\rho\left[\frac{\partial}{\partial t}(\phi\langle k\rangle^i)+\nabla\cdot(\bar{\mathbf{u}}_D\langle k\rangle^i)\right]=\nabla\cdot\left[\left(\mu+\frac{\mu_{t_\phi}}{\sigma_k}\right)\nabla(\phi\langle k\rangle^i)\right]$$
$$-\rho\phi\langle\overline{\mathbf{u}'\mathbf{u}'}\rangle^i:\nabla\bar{\mathbf{u}}_D+c_k\rho\phi\frac{\langle k\rangle^i|\bar{\mathbf{u}}_D|}{\sqrt{K}}-\rho\phi\langle\varepsilon\rangle^i \quad (20)$$

where c_k and σ_k are constants and $\rho\langle\overline{\mathbf{u}'\mathbf{u}'}\rangle^i$ is given by

$$-\rho\phi\langle\overline{\mathbf{u}'\mathbf{u}'}\rangle^i=\mu_{t_\phi}2(\bar{\mathbf{D}})^r-\frac{2}{3}\phi\rho\langle k\rangle^i\mathbf{I} \quad (21)$$

which is similar to the eddy diffusivity for microscopic flow embodied in Eq. (3). Note, however, that the coefficient μ_{t_ϕ} appearing in (21) is not necessarily the same coefficient appearing for clear fluid flow used in (3). Also, the introduced constant c_k needs to be determined for closure of the mathematical problem. The methodology established for finding it is discussed below.

The proposed model for the $\langle k\rangle^i$-equation shown above has been discussed in detail by Pedras and de Lemos [23]. For the sake of completeness, some of the ideas therein are commented on here for clarity. In [23], the influence of the porous matrix on the level of $\langle k\rangle^i$ was considered by introducing the third term on the right side of Eq. (20). In the limiting case of clear flow ($\phi\to 1\Rightarrow K\to\infty$) this extra generation rate vanishes. Under this condition, $\langle k\rangle^i$ resembles k and the transport equation for the turbulent kinetic energy in clear fluid is recovered. The physical meaning of this extra term is therefore the rate of production of $\langle k\rangle^i$ because of the presence of a porous matrix. Also, for flow through a porous bed, the amount of mechanical energy converted into turbulence is expected to depend on the medium properties. For the limiting case of high porosity and permeability media ($\phi\to 1\Rightarrow K\to\infty$), and for one-dimensional fully developed flow with a flat velocity profile, no fraction of the flow mechanical energy is expected to generate turbulence, because, in this case, the situation represents clear fluid flow. Consequently, no turbulence is generated and $\langle k\rangle^i$, if existing at the inlet, decays to zero along the flow. As the flow resistance increases, by increasing $\phi/\sqrt{K}$, gradients of local $\bar{\mathbf{u}}$ within the pore will contribute to increasing $\langle k\rangle^i$. The proposed form for the [illegible] duction term included in Eq. (20) is consistent with this expected behavior.

The macroscopic Re stresses tensor, modeled herein by (21), can be further expanded with the help of $\mathbf{u}'=\langle\mathbf{u}'\rangle^i+{}^i\mathbf{u}'$ as

$$-\rho\phi\langle\overline{\mathbf{u}'\mathbf{u}'}\rangle^i=-\rho\phi[\overline{\langle\mathbf{u}'\rangle^i\langle\mathbf{u}'\rangle^i}+\langle\overline{{}^i\mathbf{u}'\,{}^i\mathbf{u}'}\rangle^i] \quad (22)$$

The first term on the right is associated with time fluctuations $\langle\mathbf{u}'\rangle^i=\langle\mathbf{u}\rangle^{ii}$ (see Eq. (19)), whereas the second one represents the turbulent dispersion in porous medium because of both time and spatial fluctuations of the microscopic velocity. The intrinsic average for k is given here as $\langle k\rangle^i=\langle\overline{\mathbf{u}'\cdot\mathbf{u}'}\rangle^i/2$. The kinetic energy used in Refs. [8–10] differs from $\langle k\rangle^i$ and is assumed to be $k_m=\overline{\langle\mathbf{u}'\rangle^i\cdot\langle\mathbf{u}'\rangle^i}/2$. Recently, Pedras and de Lemos [17, 18] have shown the relationship between these two quan-

tities as being

$$\langle k\rangle^i = \frac{\overline{(\mathbf{u}'\cdot\mathbf{u}')}}{2} = \frac{\overline{(\mathbf{u}')^i\cdot(\mathbf{u}')^i}}{2} + \frac{\overline{(^i\mathbf{u}\cdot{}^i\mathbf{u}')^i}}{2}$$
$$= k_m + \frac{\overline{(^i\mathbf{u}'\cdot{}^i\mathbf{u}')^i}}{2} \tag{23}$$

Model Equation for $\langle\varepsilon\rangle^i$

Making use of the Dupuit–Forchheimer relationship, $\bar{\mathbf{u}}_D = \phi\langle\bar{\mathbf{u}}\rangle^i$, we propose a transport equation for $\langle\varepsilon\rangle^i$ as

$$\rho\left[\frac{\partial}{\partial t}(\phi\langle\varepsilon\rangle^i) + \nabla\cdot(\bar{\mathbf{u}}_D\langle\varepsilon\rangle^i)\right] = \nabla\cdot\left[\left(\mu + \frac{\mu_{t_\phi}}{\sigma_\varepsilon}\right)\nabla(\phi\langle\varepsilon\rangle^i)\right]$$
$$+ c_{1\varepsilon}(-\rho\overline{(\mathbf{u}'\mathbf{u}')}^i : \nabla\bar{\mathbf{u}}_D)\frac{\langle\varepsilon\rangle^i}{\langle k\rangle^i} + c_{2\varepsilon}\rho\phi\left\{c_k\frac{\langle\varepsilon\rangle^i|\bar{\mathbf{u}}_D|}{\sqrt{K}} - \frac{\langle\varepsilon\rangle^{i^2}}{\langle k\rangle^i}\right\} \tag{24}$$

where σ_ε, $c_{1\varepsilon}$, and $c_{2\varepsilon}$ are constants. As with the case of $\langle k\rangle^i$, the overall dissipation rate of $\langle\varepsilon\rangle^i$, the last term on the right side of (24), contains an additional factor that is dependent on the porous substrate. This additional term vanishes for the limiting case of clear fluid ($\phi \to 1 \Rightarrow K \to \infty$). In addition, for macroscopic fully developed unidimensional flow in isotropic and homogeneous media, the production rate of $\langle\varepsilon\rangle^i$ solely will be because of spatial deviations within the REV and will dissipated totally within the same domain. These ideas are used below when determining a numerical value for the introduced constant c_k.

Methodology for Numerically Finding c_k

As mentioned in the beginning, the objective of this work is to describe a numerical methodology with the purpose of establishing a workable turbulence model for turbulent flow in porous media. This methodology consists in finding a suitable value for the introduced constant c_k. The method adopted here consists in computing the clear flow equations (1)–(4)–(6)–(7), subjected to the adjoining equations (5)–(8)–(9), within the periodic cell in Figure 1*b*. The periodic cell represents an infinity medium, and it is characterized by an array of circular rods.

The need to compute the fine flow properties for obtaining the volume-integrated quantities has motivated the development of appropriate numerical tools. Those calculations were needed for adjusting the model and considered either the low Re k-ϵ closure [24] as well as the high Re version of it [25]. Heat transfer analysis was also the subject of additional research and preliminary results have been documented [26]. Also, the most important outcome of this development is the ability to treat hybrid computational domains with a single numerical tool [27, 28].

DISCRETIZATION OF TRANSPORT EQUATIONS

Grid Layout and Coordinate Transformation

The numerical method employed for discretizing the governing equations is the control-volume approach. For clarity, Figure 2 shows a typical control volume and includes all notation, distances, and indexing used in transforming the equations into the η-ξ coordinate system. For brevity, only the equations related to the *east* and *north* faces are presented. With the help of Figure 2, the following distances can be identified:

$$\begin{aligned} \Delta x_n^e &= (x_{ne} - x_{se}) \quad \Delta x_\xi^e = (x_E - x_P) \quad \Delta x_\eta^n = (x_N - x_P) \quad \Delta x_\xi^n = (x_{ne} - x_{nw}) \\ \Delta y_\eta^e &= (y_{ne} - y_{se}) \quad \Delta y_\xi^e = (y_E - y_P) \quad \Delta y_\eta^n = (y_N - y_P) \quad \Delta y_\xi^n = (y_{ne} - y_{nw}) \end{aligned} \tag{25}$$

With approximations in (25), the vector form of the area at the *east* and *north* faces are then given by

$$\begin{aligned} \mathbf{A}_e &= \mathbf{n}_e A_e = \Delta y_\eta^e \mathbf{e}_1 - \Delta x_\eta^e \mathbf{e}_2 \\ \mathbf{A}_n &= \mathbf{n}_n A_n = -\Delta y_\xi^n \mathbf{e}_1 + \Delta x_\xi^n \mathbf{e}_2 \end{aligned} \tag{26}$$

By definition the surface vectors are such that $(\mathbf{A}_w)_P = -(\mathbf{A}_e)_W$ and $(\mathbf{A}_s)_P = -(\mathbf{A}_n)_S$. The velocity derivatives and cross derivatives with respect to x and y, appearing

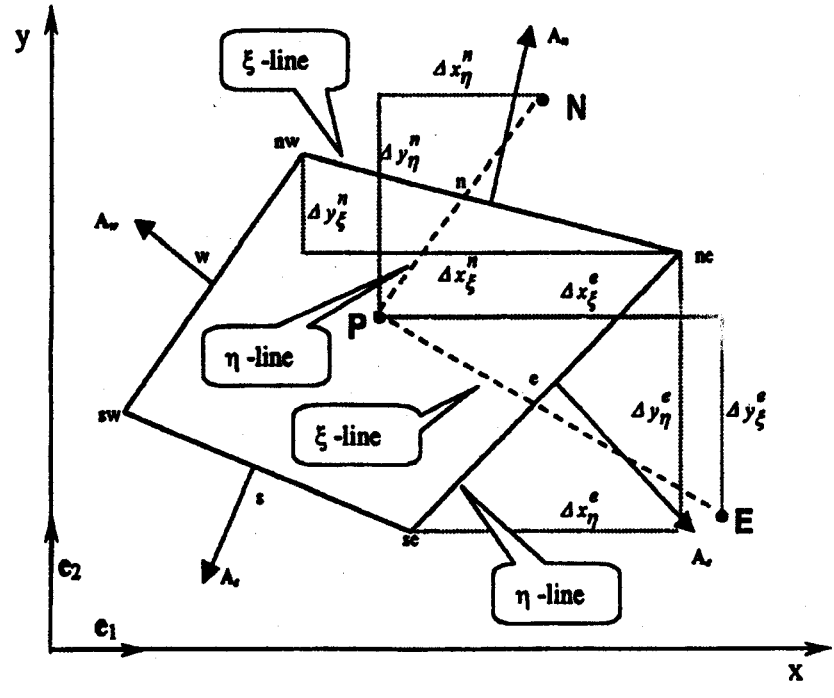

Figure 2. Control volume and notation for generalized coordinate system.

after transforming (3) into the curvilinear coordinate system ξ-η, are obtained by taking

$$\begin{aligned}
\frac{\partial U}{\partial x} &= \frac{\partial \xi}{\partial x}\frac{\partial U}{\partial \xi} + \frac{\partial \eta}{\partial x}\frac{\partial U}{\partial \eta} = \frac{1}{J}\left[\frac{\partial y}{\partial \eta}\frac{\partial U}{\partial \xi} - \frac{\partial y}{\partial \xi}\frac{\partial U}{\partial \eta}\right] \\
\frac{\partial U}{\partial y} &= \frac{\partial \eta}{\partial y}\frac{\partial U}{\partial \eta} + \frac{\partial \xi}{\partial y}\frac{\partial U}{\partial \xi} = \frac{1}{J}\left[\frac{\partial x}{\partial \xi}\frac{\partial U}{\partial \eta} - \frac{\partial x}{\partial \eta}\frac{\partial U}{\partial \xi}\right] \\
\frac{\partial V}{\partial x} &= \frac{\partial \xi}{\partial x}\frac{\partial V}{\partial \xi} + \frac{\partial \eta}{\partial x}\frac{\partial V}{\partial \eta} = \frac{1}{J}\left[\frac{\partial y}{\partial \eta}\frac{\partial V}{\partial \xi} - \frac{\partial y}{\partial \xi}\frac{\partial V}{\partial \eta}\right] \\
\frac{\partial V}{\partial y} &= \frac{\partial \eta}{\partial y}\frac{\partial V}{\partial \eta} + \frac{\partial \xi}{\partial y}\frac{\partial V}{\partial \xi} = \frac{1}{J}\left[\frac{\partial x}{\partial \xi}\frac{\partial V}{\partial \eta} - \frac{\partial x}{\partial \eta}\frac{\partial V}{\partial \xi}\right]
\end{aligned} \tag{27}$$

where J is the Jacobian of the transformation defined as

$$J = \frac{\partial x}{\partial \xi}\frac{\partial y}{\partial \eta} - \frac{\partial x}{\partial \eta}\frac{\partial y}{\partial \xi} \tag{28}$$

To obtain discrete forms of (4), both the velocity derivatives and the Jacobian have to be approximated at faces "e" and "n" of the control volume of Figure 2. Also, for a general dependent variable φ one has

$$\begin{aligned}
\left.\frac{\partial \varphi}{\partial \xi}\right|_e &\approx \frac{\varphi_E - \varphi_P}{\xi_E - \xi_P} \qquad \left.\frac{\partial \varphi}{\partial \eta}\right|_e \approx \frac{\varphi_{ne} - \varphi_{se}}{\eta_{ne} - \eta_{se}} \\
\left.\frac{\partial \varphi}{\partial \xi}\right|_n &\approx \frac{\varphi_{ne} - \varphi_{nw}}{\xi_{ne} - \xi_{nw}} \qquad \left.\frac{\partial \varphi}{\partial \eta}\right|_n \approx \frac{\varphi_N - \varphi_P}{\eta_N - \eta_P}
\end{aligned} \tag{29}$$

Here, for ease of notation, the following parameters are introduced based on the distances shown in Figure 2 at faces east "e" and north "n":

$$\begin{aligned}
\Pi_e &= \Delta y_\eta^e \Delta x_\xi^e - \Delta y_\xi^e \Delta x_\eta^e \qquad \Pi_n = \Delta y_\eta^n \Delta x_\xi^n - \Delta y_\xi^n \Delta x_\eta^n \\
\pi_a &= \Delta y_\eta^e (U_E - U_P) - \Delta y_\xi^e (U_{ne} - U_{se}) \\
\pi_a^n &= \Delta y_\eta^n (U_{ne} - U_{se}) - \Delta y_\xi^n (U_N - U_P) \\
\pi_b^e &= \Delta x_\xi^e (U_{ne} - U_{se}) - \Delta x_\eta^e (U_E - U_P) \\
\pi_b^n &= \Delta x_\xi^n (U_N - U_P) - \Delta x_\eta^n (U_{ne} - U_{nw}) \\
\pi_c^e &= \Delta y_\eta^e (V_E - V_P) - \Delta y_\xi^e (V_{ne} - V_{se}) \\
\pi_c^n &= \Delta y_\eta^n (V_{ne} - V_{nw}) - \Delta y_\xi^n (V_N - V_P) \\
\pi_d^e &= \Delta x_\xi^e (V_{ne} - V_{se}) - \Delta x_\eta^e (V_E - V_P) \\
\pi_d^e &= \Delta x_\xi^n (V_N - V_P) - \Delta x_\eta^n (V_{ne} - V_{nw})
\end{aligned} \tag{30}$$

Then using (30) to represent (28) at the east face, one has

$$\begin{aligned}
J_e &= \frac{\Delta y_\eta^e \Delta x_\xi^e - \Delta y_\xi^e \Delta x_\eta^e}{(\xi_E - \xi_P)(\eta_{ne} - \eta_{se})} = \frac{\Pi_e}{(\xi_E - \xi_P)(\eta_{ne} - \eta_{se})} \\
J_n &= \frac{\Delta y_\eta^n \Delta x_\xi^n - \Delta y_\xi^n \Delta x_\eta^n}{(\xi_{ne} - \xi_{nw})(\eta_N - \eta_P)} = \frac{\Pi_n}{(\xi_{ne} - \xi_{nw})(\eta_N - \eta_P)}
\end{aligned} \tag{31}$$

yielding for Eqs. (27) at face "e"

$$\left.\frac{\partial U}{\partial x}\right|_e \approx \frac{(y_{ne}-y_{se})(U_E-U_P)-(y_E-y_P)(U_{ne}-U_{se})}{(x_E-x_P)(y_{ne}-y_{se})-(x_{ne}-x_{se})(y_E-y_P)} = \frac{\pi_a^e}{\Pi_e}$$

$$\left.\frac{\partial U}{\partial y}\right|_e \approx \frac{(x_E-x_P)(U_{ne}-U_{se})-(x_{ne}-x_{se})(U_E-U_P)}{(x_E-x_P)(y_{ne}-y_{se})-(x_{ne}-x_{se})(y_E-y_P)} = \frac{\pi_b^e}{\Pi_e}$$

$$\left.\frac{\partial V}{\partial x}\right|_e \approx \frac{(y_{ne}-y_{se})(V_E-V_P)-(y_E-y_P)(V_{ne}-V_{se})}{(x_E-x_P)(y_{ne}-y_{se})-(x_{ne}-x_{se})(y_E-y_P)} = \frac{\pi_c^e}{\Pi_e}$$

$$\left.\frac{\partial V}{\partial y}\right|_e \approx \frac{(x_E-x_P)(V_{ne}-V_{se})-(x_{ne}-x_{se})(V_E-V_P)}{(x_E-x_P)(y_{ne}-y_{se})-(x_{ne}-x_{se})(y_E-y_P)} = \frac{\pi_d^e}{\Pi_e} \tag{32}$$

and at face "n"

$$\left.\frac{\partial U}{\partial x}\right|_n \approx \frac{(y_N-y_P)(U_{ne}-U_{nw})-(y_{ne}-y_{nw})(U_N-U_P)}{(x_{ne}-x_{nw})(y_N-y_P)-(x_N-x_P)(y_{ne}-y_{nw})} = \frac{\pi_a^n}{\Pi_n}$$

$$\left.\frac{\partial U}{\partial y}\right|_n \approx \frac{(x_{ne}-x_{nw})(U_N-U_P)-(x_N-x_P)(U_{ne}-U_{nw})}{(x_{ne}-x_{nw})(y_N-y_P)-(x_N-x_P)(y_{ne}-y_{nw})} = \frac{\pi_b^n}{\Pi_n}$$

$$\left.\frac{\partial V}{\partial x}\right|_n \approx \frac{(y_N-y_P)(V_{ne}-V_{nw})-(y_{ne}-y_{nw})(V_N-V_P)}{(x_{ne}-x_{nw})(y_N-y_P)-(x_N-x_P)(y_{ne}-y_{nw})} = \frac{\pi_c^n}{\Pi_n}$$

$$\left.\frac{\partial V}{\partial y}\right|_n \approx \frac{(x_{ne}-x_{nw})(V_N-V_P)-(x_N-x_P)(V_{ne}-V_{nw})}{(x_{ne}-x_{nw})(y_N-y_P)-(x_N-x_P)(y_{ne}-y_{nw})} = \frac{\pi_d^n}{\Pi_n} \tag{33}$$

Discretized Transport Equations

For a general dependent variable φ, in a steady state flow, a discrete form of (4) can be written as

$$I_e + I_w + I_n + I_s = S_\varphi \tag{34}$$

where I_e, I_w, I_n, and I_s are the overall fluxes (convection plus diffusion) of φ (either velocity component) at the *east*, *west*, *north*, and *south* control-volume faces, respectively, and S_φ the corresponding source term.

For the east face the flux can be written as

$$I_e = \int_{A_e} (\mathbf{n}\cdot\varphi)dA \approx (\mathbf{n}_e\cdot\varphi_e)A_e \tag{35}$$

where $\mathbf{n}_e$ is the unit vector normal to A_e and φ_e is the average value of φ prevailing at that face. Also, for coherence in the discretization process, one has for any nodal point P $(I_w)_P = -(I_e)_W$ and $(I_s)_P = -(I_n)_S$.

The numerical treatment of convection and diffusion mechanisms is handled separately. When (34) is written for the x-direction, the convection flux, I^{Cx}, has contributions from both faces *east* and *north* such as

$$I_e^{Cx} \approx F_e U_e \qquad I_n^{Cx} \approx F_N U_N \tag{36}$$

where

$$F_e = \rho[U_e\Delta y_\eta^e - V_e\Delta x_\eta^e] \quad \text{and} \quad F_n = \rho[V_n\Delta x_\xi^n - U_n\Delta y_\xi^n] \tag{37}$$

For the diffusive flux in the same x-direction, I^{Dx}, one has for the *east* and *north* faces

$$I_e^{D_x} \approx -(\mu+\mu_t)_e\left[\left(\frac{\partial U}{\partial x}+\frac{\partial U}{\partial x}\right)\mathbf{e}_1+\left(\frac{\partial U}{\partial y}+\frac{\partial V}{\partial x}\right)\mathbf{e}_2\right]_e\cdot\mathbf{A}_e$$

$$I_n^{D_x} \approx -(\mu+\mu_t)_n\left[\left(\frac{\partial U}{\partial x}+\frac{\partial U}{\partial x}\right)\mathbf{e}_1+\left(\frac{\partial U}{\partial y}+\frac{\partial V}{\partial x}\right)\mathbf{e}_2\right]_n\cdot\mathbf{A}_n \tag{38}$$

Applying coordinate transformation to (38), with the help of (30), we give a discrete form for the diffusive fluxes in the x-direction at *east* and *north* faces:

$$\begin{aligned} I_e^{D_x} \approx{}& \frac{(\mu+\mu_t)_e}{\Pi_e}\{(U_E-U_P)[2(\Delta y_\eta^e)^2+(\Delta x_\eta^e)^2] \\ &-(U_{ne}-U_{se})[2\Delta y_\xi^e\Delta y_\eta^e+\Delta x_\xi^e\Delta x_\eta^e]-\pi_c^e\Delta x_\eta^e\} \\ I_n^{D_x} \approx{}& \frac{(\mu+\mu_t)_n}{\Pi_n}\{(U_N-U_P)[2(\Delta y_\xi^n)^2+(\Delta x_\xi^n)^2] \\ &-(U_{ne}-U_{nw})[2\Delta y_\eta^n\Delta y_\xi^n+\Delta x_\eta^n\Delta x_\xi^n]-\pi_c^n\Delta x_\xi^n\} \end{aligned} \tag{39}$$

Also, for the y-momentum equation, convection and diffusive fluxes at both *east* and *north* faces as obtained in a similar fashion.

The source term because of integration of the pressure gradient term over the control volume of Figure 2 gives for the x-direction

$$S_{P_x}=-\left(\frac{\partial P}{\partial x}\right)\delta V \tag{40}$$

The gradient of P with respect to x can be approximated by using (32) as

$$\left(\frac{\partial P}{\partial x}\right)_P \approx \frac{(P_e-P_w)(y_n-y_s)-(P_n-P_s)(y_e-y_w)}{(x_e-x_w)(y_n-y_s)-(x_n-x_s)(y_e-y_w)} \tag{41}$$

The denominator in (41) is equal to the area given by the vector product of the two vectors connecting middle points of opposite control volume faces, **ew** and **ns**. Therefore, the source term for the x-momentum equation can be approximated for (40) giving a discrete form

$$S_{P_x}=-(P_e-P_w)(y_n-y_s)-(P_n-P_s)(y_e-y_w) \tag{42}$$

For improving numerical stability, the diffusion term in (39) is further rewritten as a combination of an *implicit* and an *explicit* contribution as

$$I_e^{D_x}=\underbrace{-(U_E-U_P)D_e^{x,y}}_{\text{Implicit part}}+\underbrace{S_e^{*x}}_{\text{Explicit part}} \tag{43}$$

where $D_e^{x,y}$ on the right side of Eq. (43) is a diffusion coefficient. The explicit part S_e^{*x} will make use of velocities at the grid points calculated at the previous iteration.

The production term in (6) is given by

$$P_k=\mu_t\left[2\left(\frac{\partial U}{\partial x}\right)^2+2\left(\frac{\partial V}{\partial y}\right)^2+\left(\frac{\partial U}{\partial y}+\frac{\partial V}{\partial x}\right)^2\right] \tag{44}$$

All derivatives need to be evaluated at the central point P. To this end, derivatives of the mean velocities with respect to Cartesian coordinates are transformed according

to (27). With the help of those equations and using

$$\Delta x_\eta^P = (x_n - x_s) \quad \Delta x_\xi^P = (x_e - x_w) \quad \Delta y_\eta^P = (y_n - y_s) \quad \Delta y_\xi^P = (y_e - y_w)$$

$$\Pi_P = \Delta y_\eta^P \, \Delta x_\xi^P - \Delta y_\xi^P \, \Delta x_\eta^P$$

$$\pi_a^P = \Delta y_\eta^P (U_e - U_w) - \Delta y_\xi^P (U_n - U_s)$$

$$\pi_b^P = \Delta x_\xi^P (V_n - V_s) - \Delta x_\eta^P (V_e - V_w)$$

$$\pi_c^P = \Delta x_\xi^P (U_n - U_s) - \Delta x_\eta^P (U_e - U_w)$$

$$\pi_d^P = \tilde{\Delta} y_\eta^P (V_e - V_w) - \Delta y_\xi^P (V_n - V_s)$$

finally we have a discrete expression for P_k:

$$P_k = \frac{\mu_t}{(\Pi_P)^2} [2(\pi_a^P)^2 + 2(\pi_b^P)^2 + (\pi_c^P + \pi_d^P)^2] \tag{45}$$

Values of the velocity components at cell face locations e, w, n, and s are calculated using linear interpolation.

As was done with the pressure gradient term, integration of S_φ ($\varphi = k$, ϵ; see Eqs. (6)–(7)) over the cell volume of Figure 2 surrounding point P, and already linearizing it to enhance convergence gives

$$\overline{S_\phi} \cong \int_{\delta V} S_\varphi \delta V = S_\varphi^* - S_\varphi^{**} \varphi_P \tag{46}$$

This dependence on φ_P is sometimes artificially introduced when a negative part of S_φ does not exist (Patankar, 1980 [29]). Then when the integrated source S_k is rewritten in the form of (46) one has

$$S_k^* = P_k \, \delta V \qquad -S_\kappa^{**} k = -\rho \varepsilon \delta V = -\left(\frac{\rho \varepsilon^\circ \delta V}{k^\circ}\right) k \tag{47}$$

The values of k and ε in S_k^{**} (with superscript "°" in (47)) are taken from the previous iteration and, when the solution finally converges, $k^\circ \to k$ and the two values cancel out. For S_ε, the choices for S_ε^* and S_ε^{**} are $S_\varepsilon^* = c_1 \varepsilon S_k^* / k$; $S_\varepsilon^{**} = c_2 S_k^{**}$, respectively.

NUMERICAL RESULTS AND DISCUSSION

Computation Details

As mentioned, the equations for the microscopic flow were solved numerically inside the elementary cell of Figure 1*b*. The discretized equations above were rearranged in their familiar algebraic format. The numerical method SIMPLE was employed for relaxing the mean and turbulence variables [29]. The inlet conditions on the left side were updated, after substantial residue reduction, with outlet profile on the right. This periodic boundary condition was applied repeatedly until inlet and outlet velocity profiles essentially were equal. At the top and bottom boundaries symmetry conditions were applied.

Re_H based on the cell height H varied from nearly 0.35 (creeping flow) to 1.2×10^6 (fully turbulent regime). A version of the standard k-ϵ model for high Re flow also was incorporated in the code developed. In this case, a wall function

was used for bypassing the viscous sublayer close to the wall. The nonorthogonal grid was composed of 150×100 control volumes for the high Re model and 300×200 for the low Re cases. For $Re_H = 1.2 \times 10^5$, both k-ϵ models were calculated for comparison. The dimensions of the periodic cell for the cases considered in this work were $H = 0.1$m, $S = 2H$, $D = 0.03$m ($\phi = 0.8$), 0.05m ($\phi = 0.6$), and 0.06m ($\phi = 0.4$). The solutions were grid independent, and all normalized residuals were decreased to 10^{-5}. Also, relaxation parameters for all variables ($\bar{u}$, p, k, ϵ) were kept equal to 0.8.

Eighteen case were run, including six for laminar flow, six with the low Re k-ϵ model, and six with the standard high Re closure. Porosity was varied, changing the rod diameter, and the Re was increased for the same medium porosity. A summary of all relevant parameters is presented in Table 1.

Periodic Boundary Condition

As mentioned above, the strategy for applying a periodic boundary condition to the cell of Figure 1*b* consisted in running the code several times until the inlet and outlet profiles of all variables essentially were the same. The whole algorithm considered "outer" runs and "inner" sweeps. Each "outer" run had fixed inlet values and was composed of 1000 "inner" iterations, such that the residues for all dependent variables were reduced to less than 10^{-5}. In a subsequent run, all values at outlet were plugged as boundary conditions at the inlet before another 1000 relaxation sweeps were applied again. The whole process continued until all inlet and

Table 1. Parameters for microscopic computations (velocities in m/s)

Porosity	Re_H	Turbulence model	$\langle u \rangle^i$	$\bar{u}_D$	$\langle k \rangle^i$ (m²/s²)	$\langle \epsilon \rangle^i$ (m²/s³)
$\phi = 0.40$	3.54E−01	Laminar	1.33E−05	9.30E−06	$K_{num} = 5.22E-06$ m²	
	1.20E+01	Laminar	4.50E−04	1.80E−04	$K_{eqn.\,48} = 9.44E-06$ m²	
	1.20E+04	Low Re	4.50E−01	1.80E−01	7.31E−02	1.18E+00
	1.20E+05	Low Re	4.50E+00	1.80E+00	5.92E+00	9.93E+02
	1.20E+05	High Re	4.50E+00	1.80E+00	5.71E+00	9.65E+02
	1.20E+06	High Re	4.50E+01	1.80E+01	5.81E+02	9.31E+05
$\phi = 0.60$	3.70E−01	Laminar	9.32E−06	5.54E−06	$K_{num} = 4.45E-05$ m²	
	1.20E+01	Laminar	2.99E−04	1.79E−04	$K_{eqn.\,48} = 4.84E-05$m²	
	1.20E+04	Low Re	2.99E−01	1.79E−01	3.50E−02	2.25E−01
	1.20E+05	Low Re	2.99E+00	1.79E+00	2.26E+00	1.56E+02
	1.20E+05	High Re	2.99E+00	1.79E+00	2.65E+00	1.77E+02
	1.20E+06	High Re	2.99E+01	1.79E+00	2.79E+02	1.81E+05
$\phi = 0.80$	3.88E−01	Laminar	7.20E−06	5.76E−06	$K_{num} = 1.97E-04$ m²	
	1.20E+01	Laminar	2.24E−04	1.79E−04	$K_{eqn.\,48} = 2.34E-04$ m²	
	1.20E+04	Low Re	2.24E−01	1.79E−01	1.36E−02	4.90E−02
	1.20E+05	Low Re	2.24E+00	1.79E+00	8.05E−01	3.19E+01
	1.20E+05	High Re	2.24E+00	1.79E+00	8.74E−01	3.28E+01
	1.20E+06	High Re	2.24E+01	1.79E+01	9.45E+01	3.49E+04

outlet profiles differed by not more than 0.001% Figure 3 shows the nondimensional V profiles at the outlet after each run. The figure indicates that after 4000 inner iterations the periodic condition was established., The maximum value for V along the gap was nearly 2.5% of the average axial velocity and occurred close to the wall. The nonzero values for V properly indicated the existence of a boundary layer along the gap walls.

Integral Parameters

The permeability appearing in porous media analysis (see Eqs. (20)–(24)) was calculated by solving the flow equations inside the grid of Figure 1*b*, for the Darcy regime (creeping flow, $Re_H < 1$), and also by using the expression proposed in Kuwahara et al. [12] of the form

$$K = \frac{\phi^3}{144(1-\phi)^2} D^2 \tag{48}$$

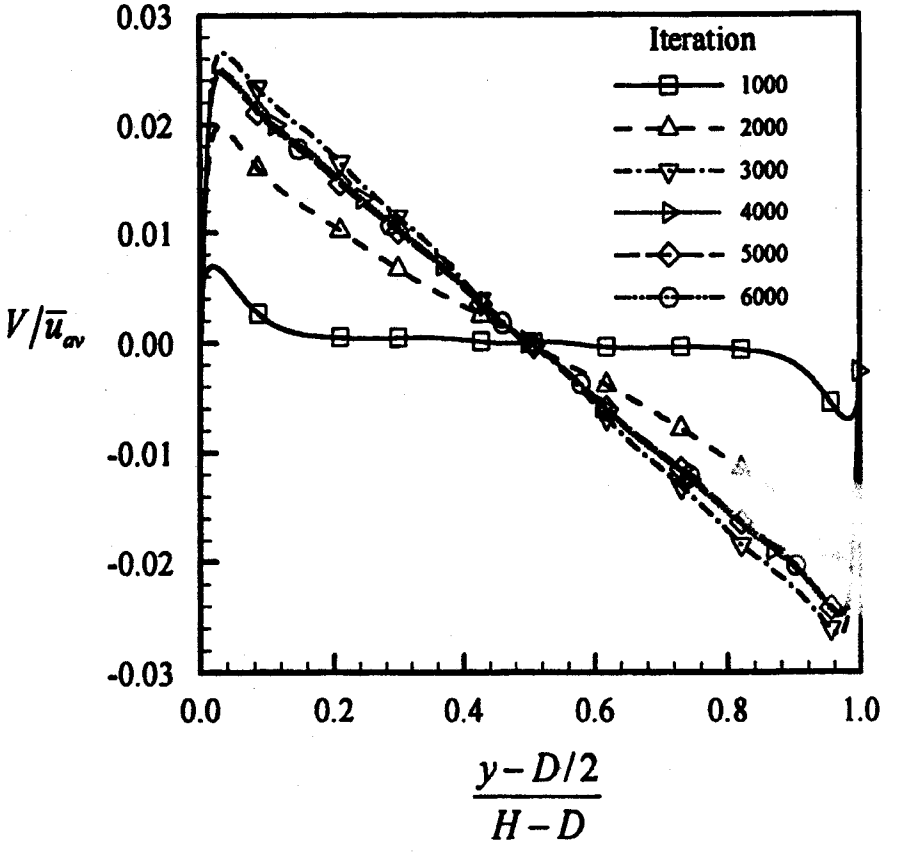

Figure 3. Nondimensional profiles for V-component at outlet of periodic cell of Figure 1*b*.

The first value was given the name K_{num} and was obtained by calculating the macroscopic pressure gradient across the periodic cell and applying it to the standard Darcy law of flow. For different porosity ϕ, a comparison with values from Eq. (48) also is presented in Table 1. Except for $\phi = 0.4$, numerical values agree well with the proposed correlation. Additional results in the table will be discussed later.

Overall pressure drop for a large range of Re_H compared with results of Kuwahara et al. [12] is presented in Figure 4. Results obtained for laminar flow and for both turbulence models used (low and high Re forms) agree well with published numerical data. Slightly lower pressure drop values show in the figure for large values of Re_H could be because of the fact that in Kuwahara et al. [12] the porous structure was simulated by an infinite array of square rods instead of cylinders as here analyzed. Flow past cylinders presents a smother flow patten, eventually implying a lower pressure drag for larger Re.

Figure 5 presents results for the effect of Re_H and ϕ on the nondimensional pressure gradient. For the same mass flow rate (same seepage velocity) the figure indicates that the pressure drop increases with the reduction of porosity. It should be pointed out that reducing ϕ implies increasing $\langle \bar{u} \rangle^i$ to keep the same Darcy velocity $\bar{u}_D$. As expected, the necessary pressure drop to overcome flow resistance is increased. Figure 6 plots results for $\langle k \rangle^i$ as a function of Re_H and ϕ. This figure (and numerical values in Table 1) further indicates that for the same Darcy velocity (Re_H = constant), or, say, the same volumetric mass flow rate through the bed, the overall integrated turbulence level increases with the reduction of the medium porosity. A faster fluid running through a narrower space will display steeper velocity gradients throughout the domain. Those gradients, in turn, dictate the rate at which the mean flow mechanical energy is transformed into turbulence energy

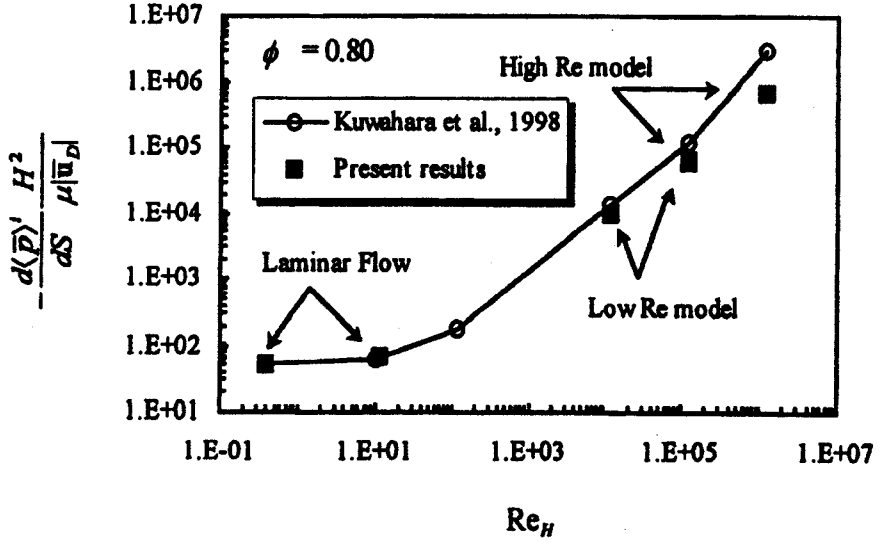

Figure 4. Overall pressure drop as a function of Re_H for the cell of Figure 1*b*.

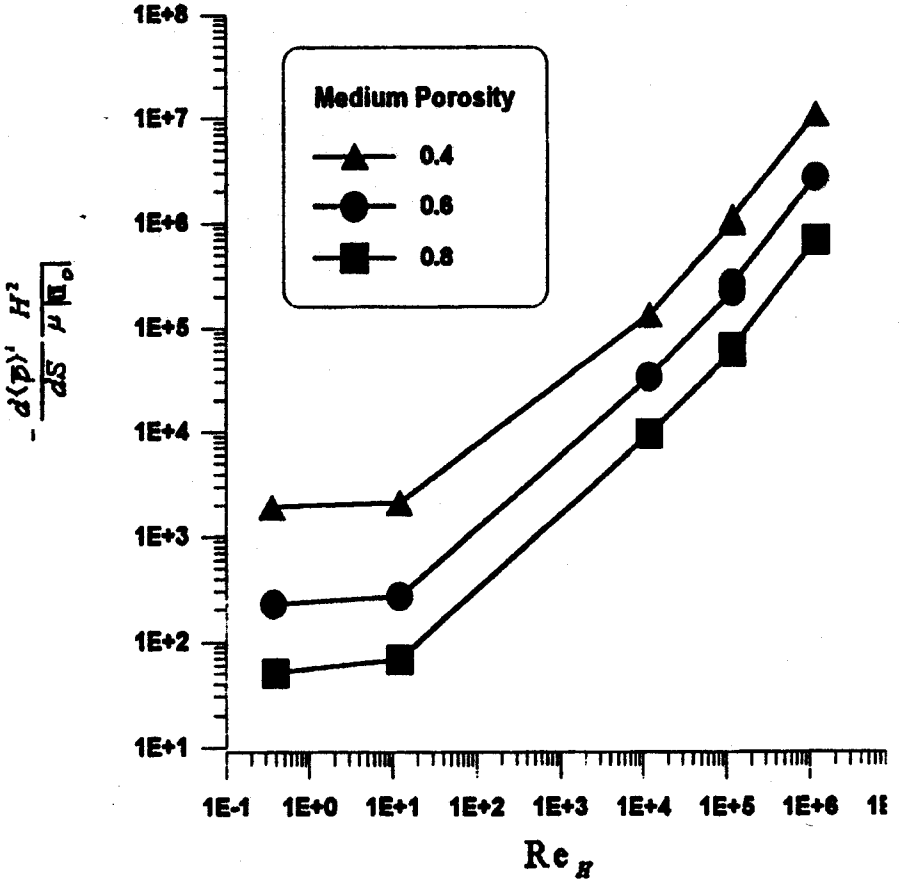

Figure 5. Nondimensional pressure gradient as a function of porosity ϕ and Re_H.

(see Eqn. (44)). Consequently, production rates of k will be higher, implying a higher value for $\langle k \rangle^I$.

Distributed Parameters

Figures 7 and 8 show $\bar{u}$ and P fields, respectively, for $Re_H = 1.2 \times 10^5$ (low Re model) and ϕ varying from 0.4 to 0.8. The vector sizes are made to be equal to enhance visualization. The flow accelerates at the upper and lower bounds of the cylinders and detaches at the rear surface. Pressure increases at the front, upper, and lower cylinder walls and recovers at the back. For lower porosity and the same mass flow rate, the size of the wake region is reduced drastically. It is important to emphasize that because of the increase in the inlet velocity, the overall pressure drop is increased rather than reduced.

Figure 9 presents similar results for k. Steeper gradients for the turbulence kinetic energy are more concentrated close to the cylinder walls as porosity decreases. This effect is observed particularly at the cylinder rear region. For lower

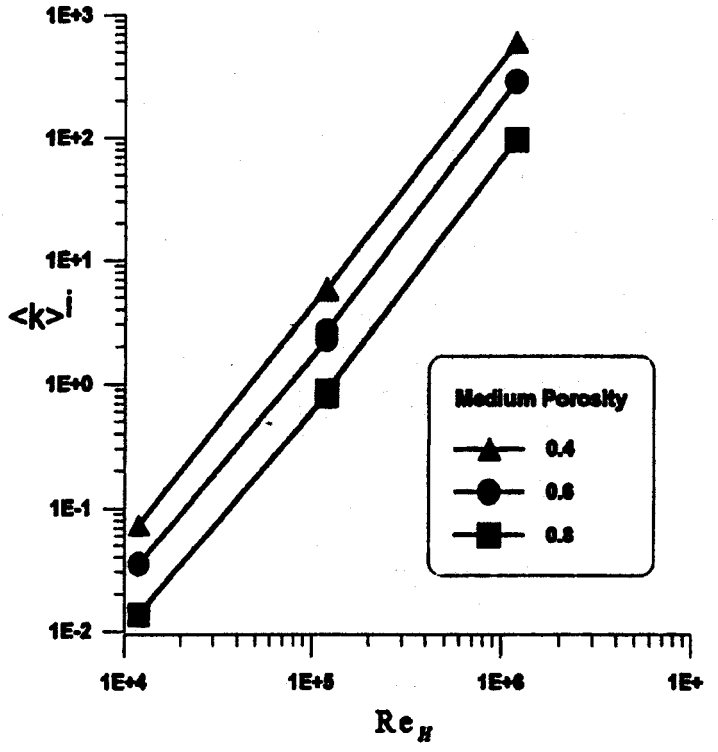

Figure 6. Variation of $\langle k \rangle^i$ as a function of porosity ϕ and Re_H.

porosity, most turbulence production occurs close to the walls rather than at the bulk of the flow. For higher ϕ, however, the existence of a wake region behind the cylinder and the lower volume occupied by the solid indicate that turbulence is produced more evenly within the flow. Kuwahara et al. [12] also observed reduction of the wake region as the porosity decreases. Figure 10 further presents the effect of Re_H on the spatial distribution of k. As can be observed in the figure, no substantial difference is detected in the distribution of the turbulence kinetic energy, although overall integral values $\langle k \rangle^i$ increase substantially with the increase of the mass flow rate. Also interesting to note is the agreement between the low and high Re k-ϵ solutions for $Re_H = 1.2 \times 10^5$ (Figures 10*b* and 10*c*), indicating the correctness of the computer code developed and accuracy of the results presented.

Constant c_k for the Macroscopic Model

Finally, the constant c_k introduced in Eq. (20) now is determined for closure of the macroscopic mathematical model proposed. For macroscopic fully developed unidimensional flow in isotropic and homogeneous media the limiting values for $\langle k \rangle^i$ and $\langle \varepsilon \rangle^i$ in the additional terms introduced in Eqs. (20) and (24) are given the values k_ϕ and ε_ϕ, respectively. In this limiting condition, Eqs. (20) and (24) both

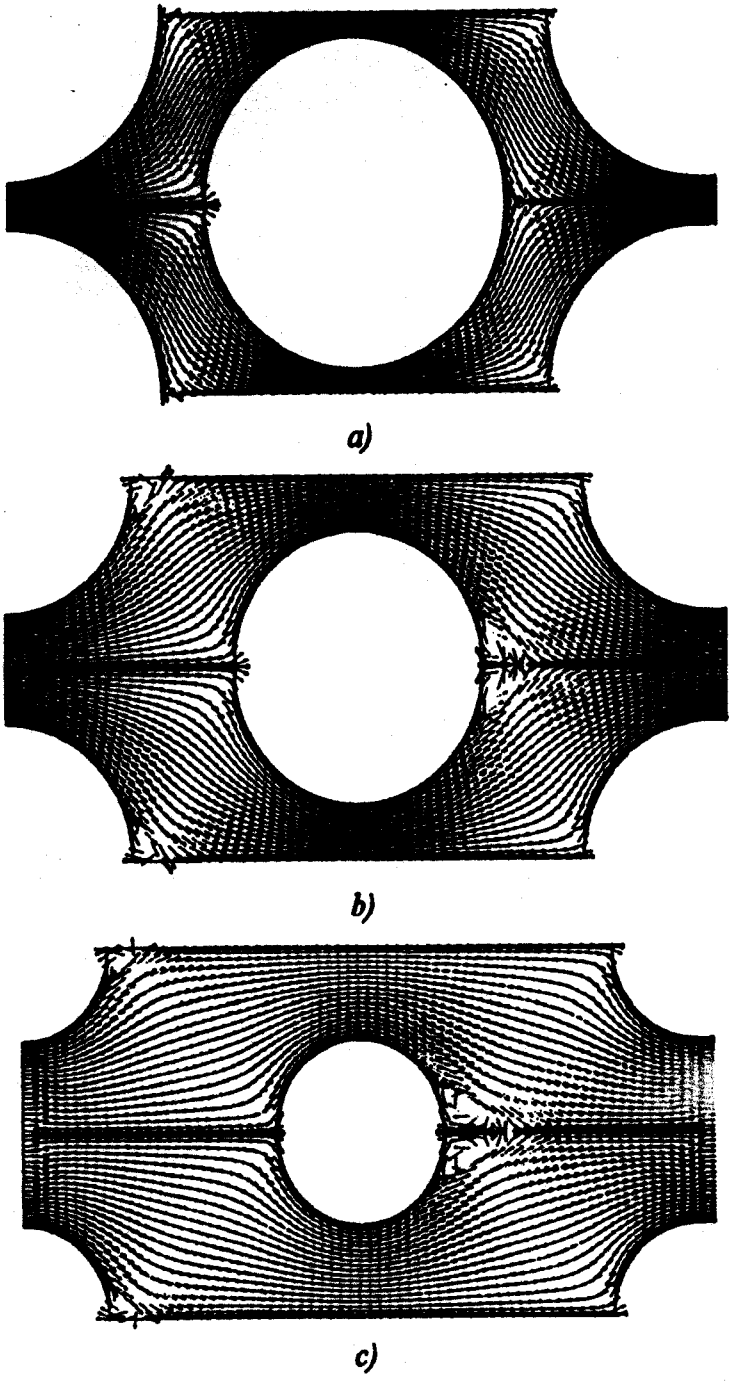

Figure 7. Vector plots ($Re_H = 1.2 \times 10^5$): (*a*) $\phi = 0.4$; (*b*) $\phi = 0.6$; (*c*) $\phi = 0.8$.

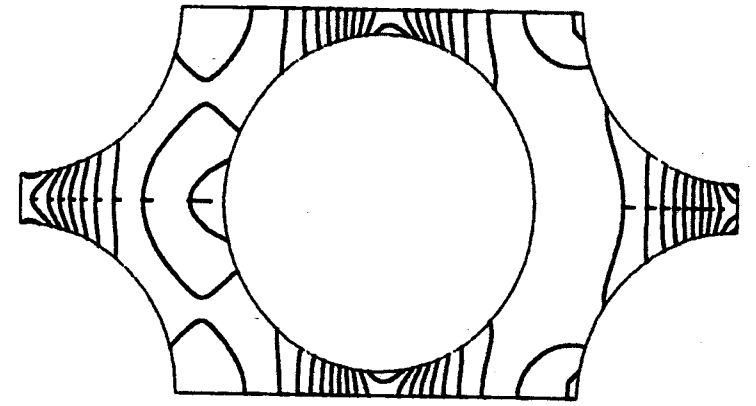

a)

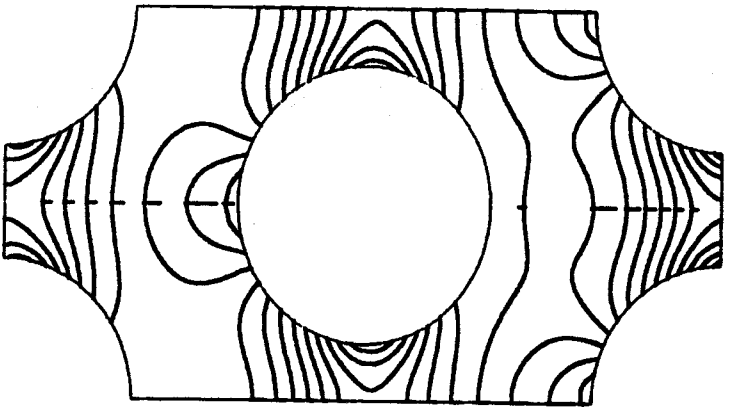

b)

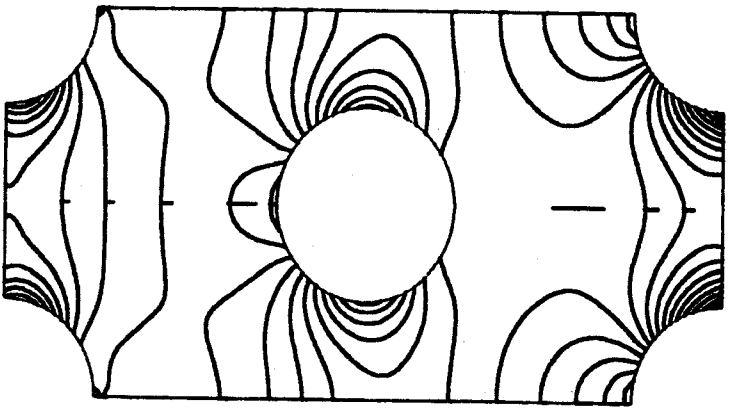

c)

Figure 8. Pressure contours ($Re_H = 1.2 \times 10^5$): (*a*) $\phi = 0.4$, (*b*) $\phi = 0.6$, (*c*) $\phi = 0.8$.

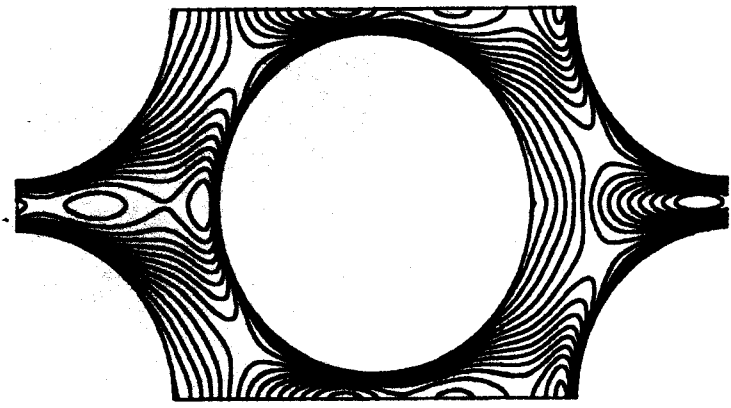

a)

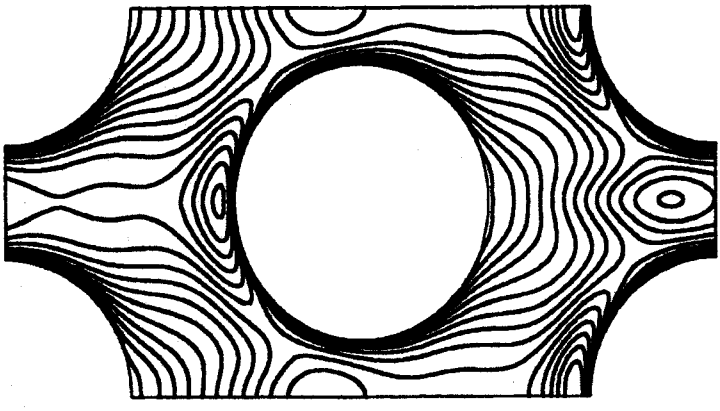

b)

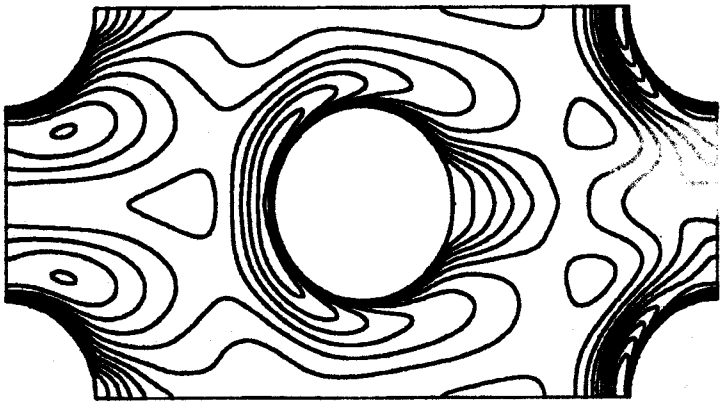

c)

Figure 9. Contour plots for $\langle k \rangle^i (\mathrm{Re}_H = 1.2 \times 10^5)$: (*a*) $\phi = 0.4$; (*b*) $\phi = 0.6$; (*c*) $\phi = 0.8$.

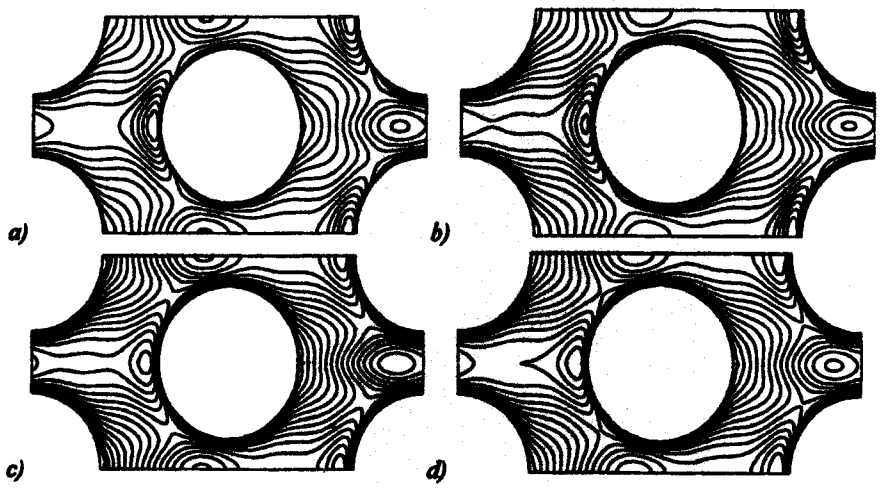

Figure 10. Effect of mass flow rate on $\langle k \rangle^l$ ($\phi = 0.60$): (*a*) $Re_H = 1.2 \times 10^4$ low Re; (*b*) $Re_H = 1.2 \times 10^5$ low Re, (*c*) $Re_H = 1.2 \times 10^5$ high Re; (*d*) $Re_H = 1.2 \times 10^6$ high Re.

will reduce to the situation where production and dissipation rates balance each other. Using then the limiting cases k_ϕ and ε_ϕ, we can combine both Eqs. (20) and (24), in this situation, into the nondimensional form

$$\frac{\varepsilon_\phi \sqrt{K}}{|\bar{u}_D|^3} = c_k \frac{k_\phi}{|\bar{u}_D|^2} \tag{49}$$

To obtain c_k, the microscopic computations described above for different porosity and Re_H were used to calculate the corresponding limiting values k_ϕ and ε_ϕ (also seen in Table 1 under the notation $\langle k \rangle^l$ and $\langle \varepsilon \rangle^l$, respectively). Once these intrinsic values were obtained, they were plugged into Eq. (49) with the permeability calculated by (48). The value of c_k equal to 0.28 was found by noting the collapse of all data into the straight line shown in Figure 11. Also interesting point out is that, under the macroscopic model proposed here, a unique value for c_k was found to be adequate for a wide range of porosity and Re. Accordingly, little spreading of computed values is observed around the straight line of Figure 11.

Note also that the figure shows corresponding results by Nakayama an Kuwahara [15]. In that work, a different methodology was employed, and expressions for k_ϕ and ε_ϕ as functions of ϕ were proposed. Therefore, for a certain porosity, the relationships in Nakayama and Kuwahara [15] allow for the calculation of k_ϕ and ε_ϕ. When plotted in Figure 11, these pairs $k_\phi - \varepsilon_\phi$ also seem to follow the same straight line (see solid symbols in the figure). This agreement indicates the appropriateness of the methodology proposed here and gives support to the modeling ideas presented here.

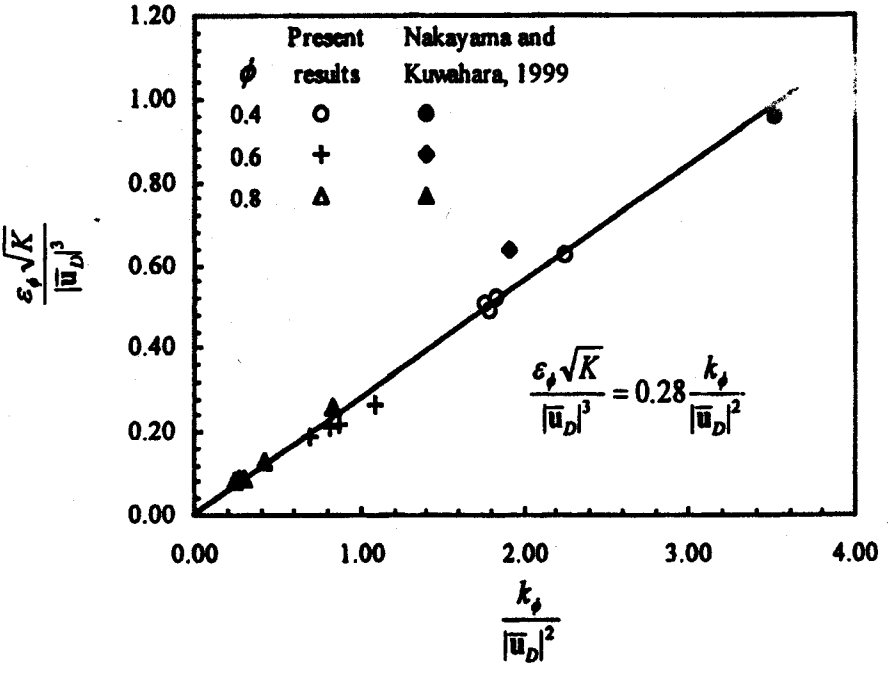

Figure 11. Determination of value for c_k using data for different porosity and Re.

CONCLUDING REMARKS

This work presented the numerical solution of the flow governing equations in a domain used to represent porous media. The low Re turbulence model as well as the high Re version of the k-ϵ closure were applied. A proposal for a macroscopic turbulence model based on volume integration of clear fluid equations was carried out. Additional terms accounting for the presence of the solid matrix were introduced along with an additional constant to be determined.

The computations showed that for small values of porosity the level of turbulence kinetic energy is increased. For low porosity, concentration of turbulence production close to solid surfaces was observed and nearly no recirculating motion behind the cylinder was detected. In addition, no substantial differences in the spatial distribution of normalized k were observed for different incoming mass flow rates.

The methodology followed for determining the introduced constant c_k consisted in solving first the clear fluid equations within a periodic cell. Integrated parameters considering different porosity and Re number then were used to establish a numerical value for the proposed constant.

REFERENCES

1. H. Darcy, Les Fontaines Publiques de la Vile de Dijon, Victor Dalmond, Paris, 1856.
2. P. Forchheimer, Wasserbewegung durch Boden, *Z. Ver. Deutsch. Ing.*, vol. 45, pp. 1782–1788, 1901.

3. H. C. Brinkman, A Calculation of the Viscous Force Exerted by a Flowing Fluid on a Dense Swarm of Particles, *Appl. Sci. Research*, vol. A1, pp. 27–34, 1947.
4. J. C. Ward, Turbulent Flow in Porous Media, *J. Hydraul. Div. ASCE*, vol. 90, part HY5, pp. 1–12, 1964.
5. S. Whitaker, Advances in Theory of Fluid Motion in Porous Media, *Indust. Engng. Chem., vol. 61, pp. 14–28, 1969.*
6. J. Bear, Dynamics of Fluids in Porous Media, Elsevier, New York, 1972.
7. K. Vafai and C. L. Tien, Boundary and Inertia Effects on Flow and Heat Transfer in Porous Media, *Int. J. Heat Mass Transfer*, vol. 24, pp. 195–203, 1981.
8. K. Lee and J. R. Howell, Forced convective and radiative transfer within a highly porous layer exposed to a turbulent external flow field, in *Proc. 1987 ASME-JSME Thermal Engineering Joint Conf.*, vol. 2, pp. 377–386, 1987.
9. H. Wang and E. S. Takle, Boundary-Layer Flow and Turbulence Near Porous Obstacles, *Boundary Layer Meteorology*, vol. 74, pp. 73–88, 1995.
10. B. V. Antohe and J. L. Lage, A General Two-Equation Macroscopic Turbulence Model for Incompressible Flow in Porous Media, *Int. J. Heat Mass Transfer*, vol. 40, pp. 3013–3024, 1997.
11. T. Masuoka and Y. Takatsu, Turbulence Model for Flow through Porous Media. *Int. J. Heat mass Transfer*, vol. 39, pp. 2803–2809, 1996.
12. F. Kuwahara, Y. Kameyama, S. Yamashita, and A. Nakayama, Numerical Modeling of Turbulent Flow in Porous Media Using a Spatially Periodic Array, *J. Porous Media*, vol. 1, pp. 47–55, 1998.
13. F. Kuwahara and A. Nakayama, Numerical Modeling of Non-Darcy Convective Flow in a Porous Medium, in *Heat Transfer 1998: Proc. 11th Int. Heat Transfer Conf.*, Kyongju, Korea, vol. 4, pp. 411–416, Taylor & Francis, Washington, DC, 1998.
14. Y. Takatsu and T. Masuoka, Turbulent Phenomena in Flow through Porous Media, *J. Porous Media*, vol. 3, pp. 243–251, 1998.
15. A Nakayama and F. Kuwahara, A Macroscopic Turbulence Model for Flow in a Porous Medium, ASME *Journal of Fluids Engineering*, vol. 121, pp. 427–433, 1999.
16. V. S. Travkin, K. Hu, and I. Catton, Turbulent Kinetic Energy and Dissipation Rate Equation Models for Momentum Transport in Porous Media, in *Proc. 3rd ASME/JSME Joint Fluids Engineering Conference* (on CD-ROM), Paper FEDSM99-7275, San Francisco, CA, 1999.
17. M. H. J. Pedras and M. J. S. de Lemos, On Volume and Time Averaging of Transport Equations for Turbulent Flow in Porous Media, in *Proc. 3rd ASME/JSME Joint Fluids Engineering Conference* (on CD-ROM), Paper FEDSM99-7273, San Francisco, CA, 1999.
18. M. H. J. Pedras and M. J. S. de Lemos, On the Definition of Turbulent Kinetic Energy for Flow in Porous Media, *Int. Comm. in Heat & Mass Transfer*, vol. 27, no. 2, pp. 211–220, 2000.
19. W. G. Gray and P. C. Y. Lee, On the Theorems for Local Volume Averaging of Multiphase System, *Int. J. Multiphase Flow*, vol. 3, pp. 333–340, 1977.
20. K. Abe, Y. Nagano, and T. Kondoh, An Improved k-ϵ Model for Prediction of Turbulent Flows with Separation and Reattachment, *Trans. JSME*, Ser. B, vol. 58, no. 554, pp. 3003–3010, 1992.
21. J. C. Slattery, Flow of Viscoelastic Fluids through Porous Media, *A.I.Ch.E. J.*, vol. 13, pp. 1066–1071, 1967.
22. M. H. J. Pedras and M. J. S. de Lemos, Macroscopic Turbulence Modeling for Saturated Porous Media, in *Proc. of COBEM99—15th Braz. Congr. Mech. Eng.* (on CD-ROM), ISBN: 85-85769-03-3, Águas de Lindóia, São Paulo, Brazil, 1999 (in Portuguese).

23. M. H. J. Pedras and M. J. S. de Lemos, Macroscopic Turbulence Modeling for Incompressible Flow through Undeformable Porous Media, *Intern. J. Heat and Mass Transfer*, vol. 44, pp. 1081–1993, 2001.
24. M. H. J. Pedras and M. J. S. de Lemos, Numerical Solution of Turbulent Flow in Porous Media Using a Spatially Periodic Cell and the Low Reynolds k-ϵ Model, in *Proc. CONEM2000—National Mechanical Engineering Congress* (on CD-ROM), Natal, Rio Grande do Norte, Brazil, 2000 (in Portuguese).
25. F. D. Rocamora Jr. and M. J. S. de Lemos, Numerical Solution of Turbulent Flow in Porous Media Using a Spatially Periodic Array and the k-ϵ Model, in *Proc. ENCIT-98—7th. Braz. Cong. Eng. Th. Sci.*, vol. 2, pp. 1265–1271, Rio de janeiro, RJ, Brazil, 1998.
26. F. D. Rocamora Jr. and M. J. S. de Lemos, Simulation of Turbulent Heat Transfer in Porous Media Using a Spatially Periodic Cell and the k-ϵ Model, in *Prof. COBEM99—15th Braz. Congr. Mech. Eng.* (on CD-ROM), ISBN: 85-85769-03-3, Águas de Lindóia, São Paulo, Brazil, 1999.
27. F. D. Rocamora Jr. and M. J. S. de Lemos, Prediction of Velocity and Temperature Profiles for Hybrid Porous Medium-Clean Fluid Domains, in *Proc. CONEM2000—National Mechanical Engineering Congress*, Natal, Rio Grande do Norte, Brazil, 2000.
28. F. D. Rocamora Jr. and M. J. S. de Lemos, Laminar Recirculating Flow and Heat Transfer in Hybrid Porous Medium-Clear Fluid Computational Domains, in *Proc. 34th ASME—National Heat Transfer Conference*, Paper NHTC2000-12317, Pittsburgh, PA, 2000.
29. S. V. Patankar, Numerical Heat Transfer and Fluid Flow, Mc-Graw, Hill, New York, 1980.